Achieving irradiation-resistant metallic alloys by immobilizing induced defects

Shasha Huang [a], Zhengxiong Su [b], Shihua Ma [a], Baichuan Xu [a], Haijun Fu [a], Xuepeng Xiang [a], Wenyu Lu [a], Ailin Yang [a], Zhongtao Li [c], Sergei L. Dudarev [d], Chenyang Lu [b,], Zhenggang Wu [c,*], Shijun Zhao [a, e,*]*

[a] Department of Mechanical Engineering, City University of Hong Kong, Hong Kong, China

[b] Department of Nuclear Science and Technology, Xi'an Jiaotong University, Xi'an, 710049, China

[c] College of Materials Science and Engineering, Hunan University, Changsha 410082, China

[d] UK Atomic Energy Authority, Culham Science Centre, Abingdon, OX14 3DB, UK

[e] Department of Materials Science and Engineering, City University of Hong Kong, Hong Kong, China

Corresponding author: shijzhao@cityu.edu.hk, zwu9@hnu.edu.cn, chenylu@xjtu.edu.cn

Supplementary Information

Table of Contents

Table of Supplementary Tables

Table of Supplementary Figures

Supplementary Note I. Local lattice distortion

The radial displacement method was employed to quantify the local lattice distortion of the alloys. The results are displayed in **Supplementary Fig. 1**. The average deviation of each component is also shown in the figure. Notably, the extent of local lattice distortion exhibits the broadest range in the $Ni_{80}Mo_{20}$, diminishing sequentially in NiCoV and NiFe. Mo atoms manifest the most pronounced distortion relative to other elemental constituents within these alloys. Furthermore, the introduction of V into the Ni matrix emerges as a more effective strategy for inducing significant lattice distortion than the incorporation of Fe and Co.

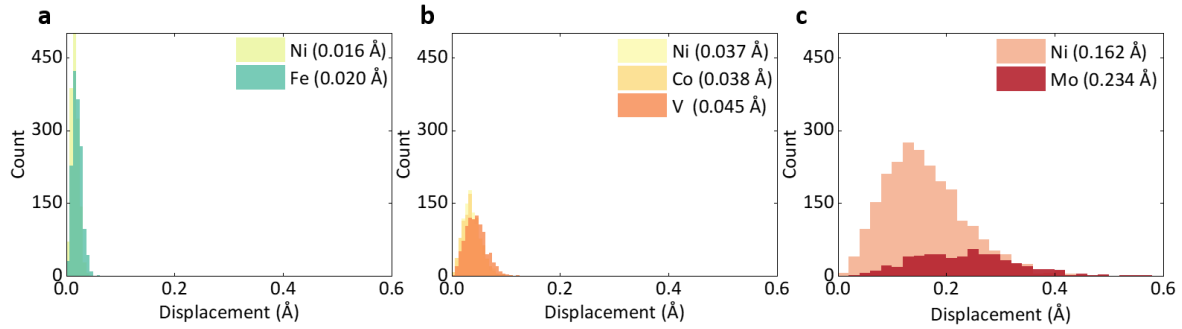

Supplementary Fig. 1. Atomic radial displacement in **a,** NiFe, **b,** NiCoV, and **c,** $Ni_{80}Mo_{20}$.

Supplementary Note II. Defect cluster binding energies and diffusion trajectories

Supplementary Fig. 2 shows the cluster binding energies of 1/3<111> interstitial-type dislocation loops and voids, respectively. These structures are commonly observed in FCC materials after irradiation[1]. The cluster binding energies are defined as $E_b^{N+1} = E^N + E^1 - E^{N+1} - E^{bulk}$, where E^N and E^{N+1} represent the total energies of cells containing a cluster of size N and N+1, respectively. E^{bulk} and E^1 correspond to the total energies of the perfect cell and the cell containing a point defect, respectively. E_b^{N+1} denotes the binding energy of a point defect attaching to a cluster of size N. According to this definition, a higher binding energy indicates a more favorable formation of larger clusters. The results presented are averaged from 10 independent calculations.

The interstitial binding energies depicted in **Supplementary Fig. 2a** show that Ni has the highest binding energy among the alloys, consistent with previous studies[1]. This finding qualitatively matches our observations, where the largest interstitial cluster is found in Ni. Additionally, **Supplementary Fig. 2a** demonstrates that interstitial cluster size tends to decrease with increasing lattice distortion, with the smallest clusters observed in $Ni_{80}Mo_{20}$, aligning with our results in **Fig. 1d** and **Fig. 2b**. In contrast, **Supplementary Fig. 2b** reveals no significant differences in the vacancy-type cluster binding energies among the four materials.

Therefore, cluster binding energies do not appear to explain the observed variations in vacancy cluster distributions.

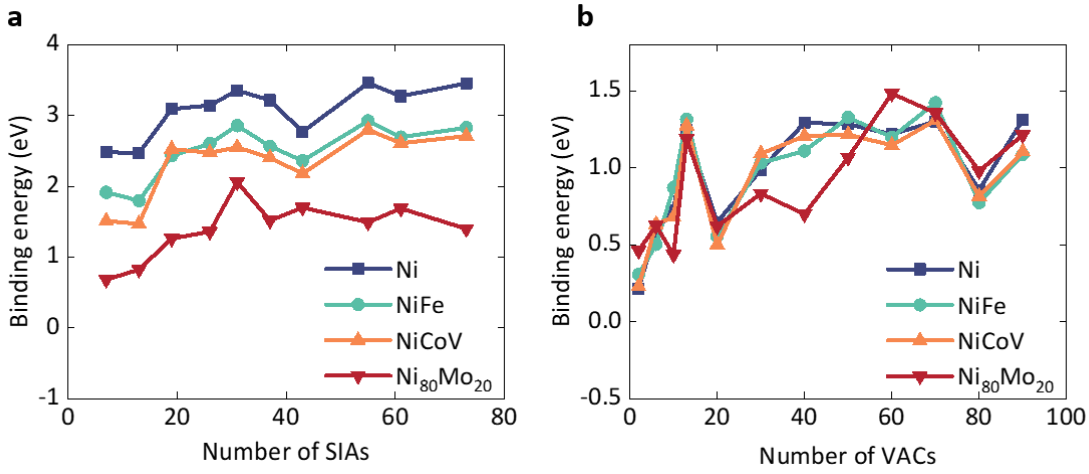

Supplementary Fig. 2. a, Interstitial- and **b,** vacancy-type cluster binding energies in the four materials.

Supplementary Fig. 3 presents the diffusion trajectory of a size 10 interstitial- or vacancy-type cluster in the four materials. With increasing lattice distortion, long-range motion of interstitial migration is inhibited while the vacancy migration is promoted. However, in $Ni_{80}Mo_{20}$, both the interstitial and vacancy migration are significantly frozen.

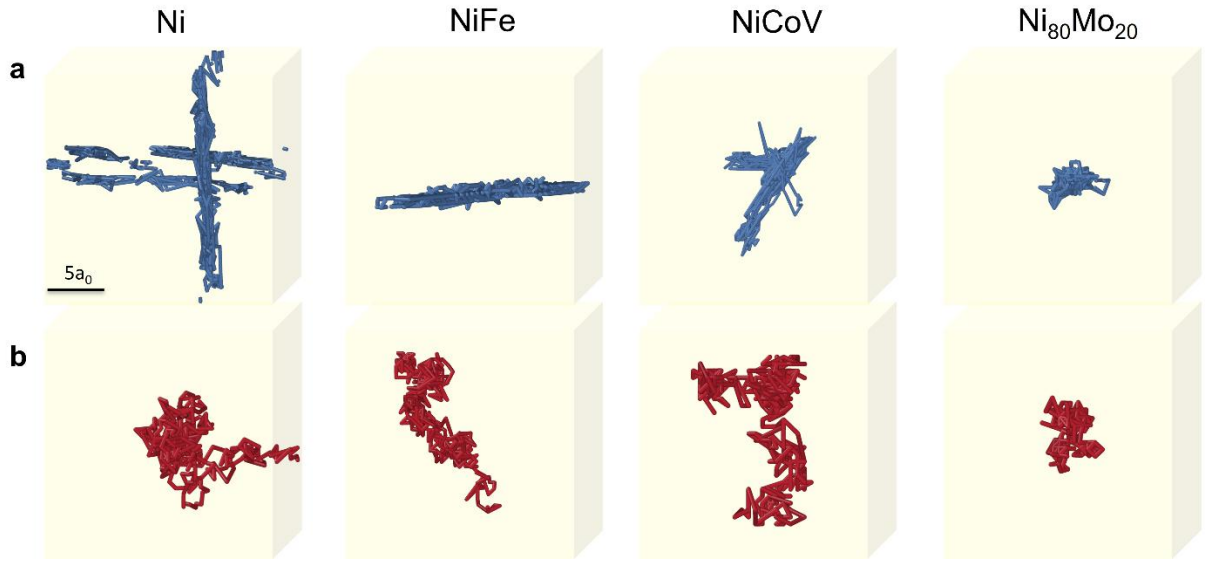

Supplementary Fig. 3. Trajectory of a size 10 **a,** interstitial cluster simulated at 1000 K for 5 ns and **b,** vacancy cluster simulated at 1000 K for 5 ns. The scale bar in the first panel applies to all images in (a) and (b), a_0 is the lattice constant for each alloy.

Supplementary Note III. Mechanism governing defect diffusion

The defect formation and migration energies in these alloys are shown in **Supplementary Fig. 4**. The corresponding formation energies of interstitial and vacancy in pure Ni are indicated by grey dash lines, with the specific values labeled in grey text. The obtained defect energetics reveals that the increased local lattice distortion significantly broadens the range of defect formation energies to even over 4 eV. Moreover, a comparison between **Supplementary Fig. 4a-c** and **Supplementary Fig. 4d-f** demonstrates that increasing lattice distortion can lead to a substantial overlap of interstitial and vacancy formation energies, even in the absence of strong chemical complexity. The vacancy migration energies are elucidated in **Supplementary Fig. 4g-i**, with the value of pure Ni indicated by the grey dashed line and grey text. The results reveal that an increase in local lattice distortion correlates with a reduction and wider distribution in vacancy migration energies. Besides, the average migration energy decreases with the increase of local lattice distortion, indicating an enhanced vacancy migration. In $Ni_{80}Mo_{20}$, it is noteworthy that some vacancy formation and migration energies are observed to be 0 eV. The zero values may arise from using the chemical potential of BCC Mo in the defect formation energy calculations. Moreover, previous studies suggest that severe lattice distortions can lower the vacancy migration barrier to 0 eV, potentially enhancing vacancy mobility[2,3].

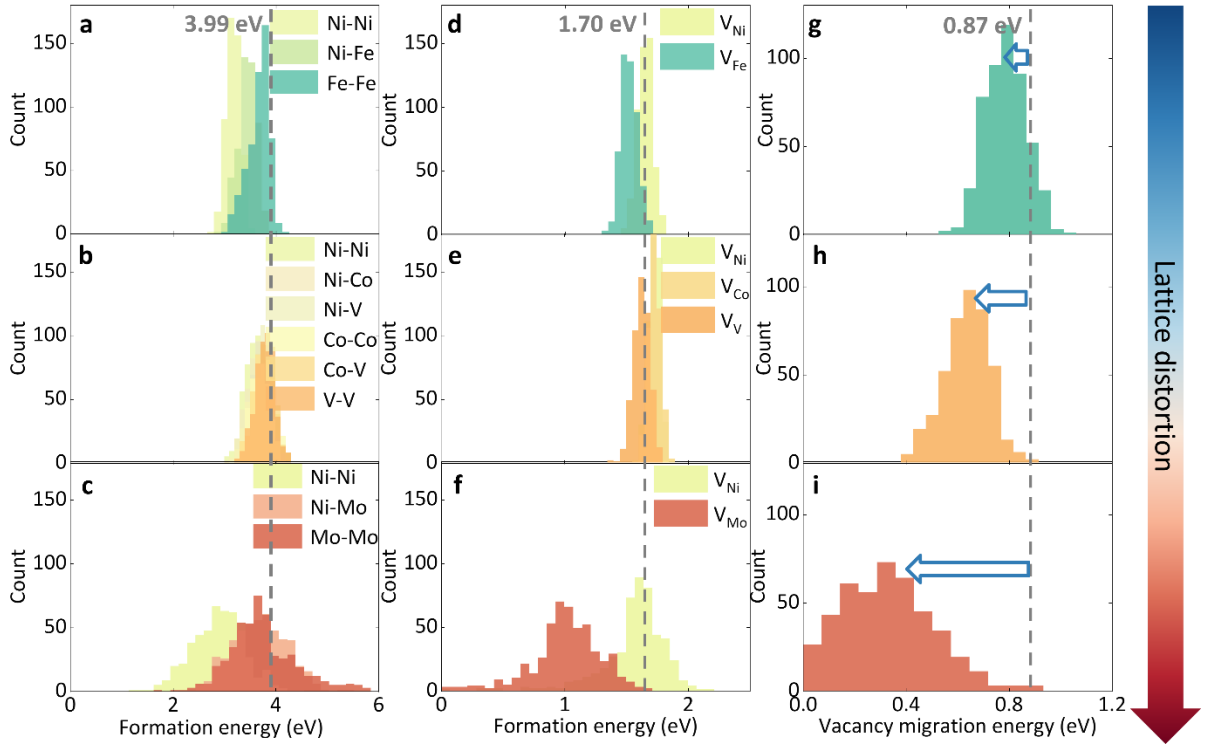

Supplementary Fig. 4. Distribution of dumbbell formation energies in **a,** NiFe, **b,** NiCoV, and

c, $Ni_{80}Mo_{20}$; vacancy (V) formation energies in **d,** NiFe, **e,** NiCoV, and **f,** $Ni_{80}Mo_{20}$; and vacancy migration energies in **g,** NiFe, **h,** NiCoV, and **i,** $Ni_{80}Mo_{20}$. The corresponding defect formation and migration energies in pure Ni are indicated by grey dashed lines and text.

Supplementary Fig. 5 presents the distribution of $\cos(\theta)$ and corresponding correlation factor f_v in Ni, NiFe, NiCoV, and $Ni_{80}Mo_{20}$. In pure Ni, the distribution of $\cos(\theta)$ is nearly symmetric around zero, yielding an average value of zero and a f_v of 1, corresponding to a random walk. When alloying with other elements, the correlation factor begins to deviate from 1. Specifically, in the highly distorted $Ni_{80}Mo_{20}$, most $\cos(\theta)$ values are -1, indicating that vacancies jump back and forth in their positions without significant net displacement.

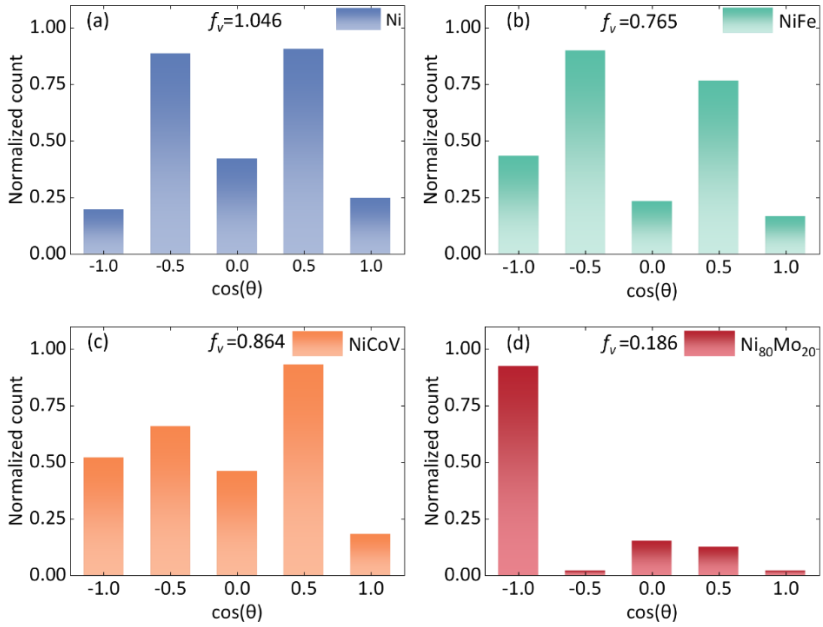

Supplementary Fig. 5. Distribution of $\cos(\theta)$ in **a,** Ni, **b,** NiFe, **c,** NiCoV, and **d,** $Ni_{80}Mo_{20}$ in 50 ns vacancy diffusion at 1000 K. The calculated correlation factors are also indicated.

Supplementary Note IV. Defect localization induced by lattice distortions

To distinguish the effect of chemical complexity and lattice distortion on controlling defect diffusion, a series of Ni-Mo alloys were selected to study the defect diffusion behaviors. The selected Ni-Mo alloys and their corresponding atomic size mismatches are presented in **Supplementary Table 1**.

Supplementary Table 1. Atomic size mismatch (δ%) in $Ni_{100-x}Mo_x$ alloys.

	$Ni_{99}Mo_1$	$Ni_{98}Mo_2$	$Ni_{94}Mo_6$	$Ni_{90}Mo_{10}$	$Ni_{85}Mo_{15}$
δ(%)	1.23	1.73	3.18	3.66	4.33

Supplementary Fig. 6 illustrates the single interstitial and vacancy diffusion trajectories in $Ni_{100-x}Mo_x$ alloys at 1000 K. The increase in lattice distortion by doping more Mo content led to the inhibited interstitial diffusion. However, the vacancy mobility showed a first increased and then decreased tendency with the increase of lattice distortion.

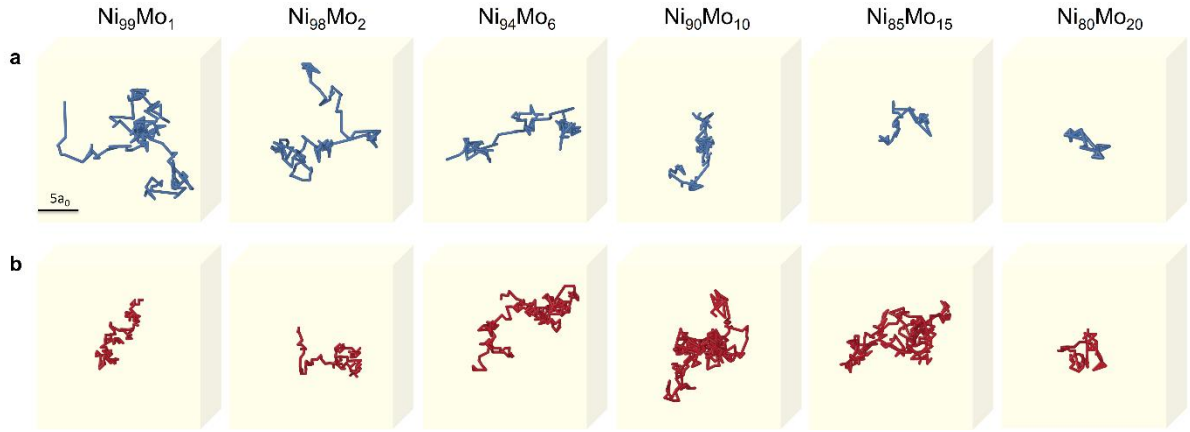

Supplementary Fig. 6. Trajectory of **a,** single interstitial simulated at 1000 K for 500 ps and **b,** single vacancy simulated at 1000 K for 5 ns in in Ni-Mo alloys. The scale bar in the first panel applies to all images.

Supplementary Note V. Competition between reduced barrier and strengthened trapping

Supplementary Table 2 shows the distribution of vacancy migration barriers and initial state energies in the Ni-Mo alloys. These values, including the mean and standard error, were derived from 5,000 independent NEB simulations.

Supplementary Table 2. Distribution of vacancy migration barriers (μ_{E_s} and σ_{E_s}) and the distribution of initial state energies (μ_{E_0} and σ_{E_0}). These energies are classified according to

the type of X atom exchanged with the vacancy, X can be Ni or Mo.

	μ_{E_s} (Ni)	σ_{E_s} (Ni)	μ_{E_s} (Mo)	σ_{E_s} (Mo)	μ_{E_0} (Ni)	σ_{E_0} (Ni)	μ_{E_0} (Mo)	σ_{E_0} (Mo)
$Ni_{99}Mo_1$	0.82	0.05	0.62	0.08	0.0044	0.0232	0.0010	0.0327
$Ni_{98}Mo_2$	0.80	0.07	0.61	0.11	0.0024	0.0376	0.0036	0.0518
$Ni_{94}Mo_6$	0.68	0.11	0.57	0.17	0.0121	0.0620	0.0035	0.0977
$Ni_{90}Mo_{10}$	0.57	0.14	0.55	0.21	0.0354	0.0886	0.0259	0.1382
$Ni_{85}Mo_{15}$	0.44	0.16	0.54	0.27	0.0407	0.1323	0.0030	0.1976
$Ni_{80}Mo_{20}$	0.30	0.21	0.56	0.32	0.0941	0.2345	0.0406	0.3000

Vacancy diffusion is influenced by both kinetic and thermodynamic factors, and their dependence on Mo concentration is illustrated in **Supplementary Fig. 7**. In particular, when the Mo concentration exceeds 15% (resulting in a lattice distortion greater than 4.33%), the thermodynamic factor becomes substantially lower—and even negative—relative to the kinetic factor, thereby decreasing the likelihood of vacancy net forward diffusion. This behavior is attributed to the marked broadening of σ_{E_0} as shown in **Supplementary Table 2**

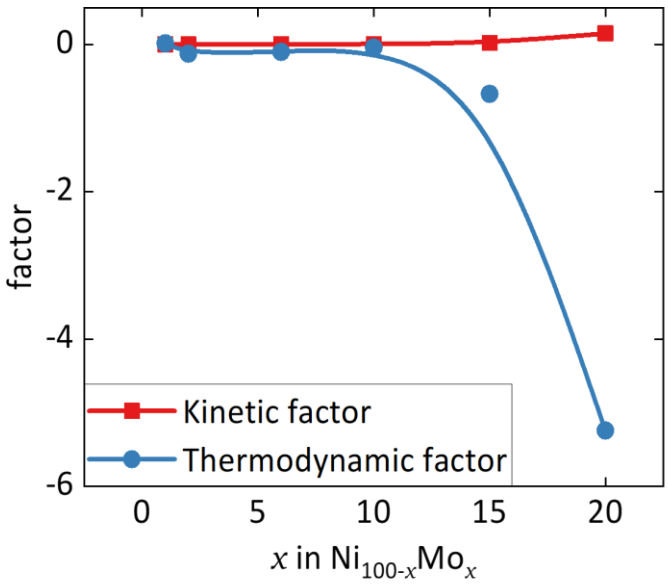

Supplementary Fig. 7. Evolution of kinetic and thermodynamic factors under different Mo

concentrations.

Supplementary Note VI. Increase σ_{E_0} to constrain vacancy migration

Supplementary Fig. 8 depicts the displacement of 1NN atoms of vacancy in $Ni_{100-x}Mo_x$ alloys in initial and final states. The results show that the increase of lattice distortion not only leads to an increase in the mean value of 1NN atom displacement but also widens their distribution.

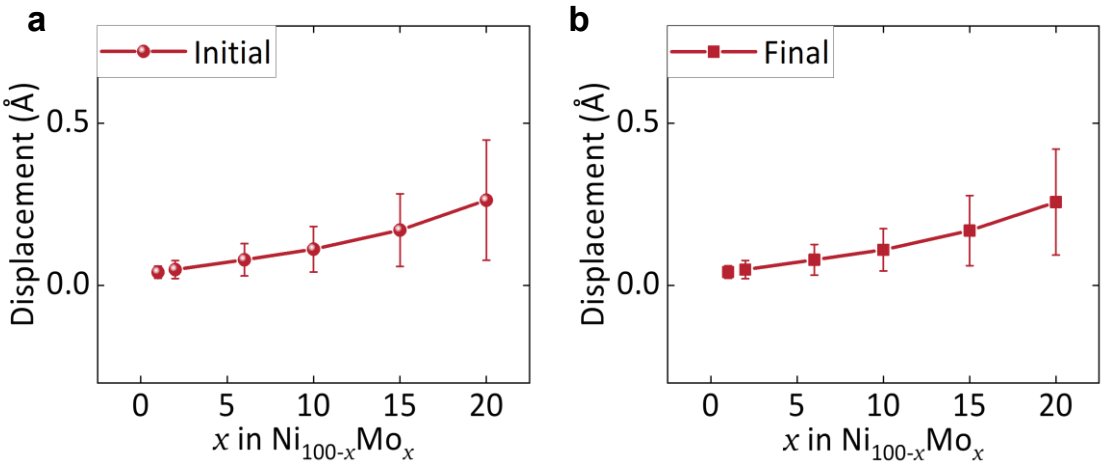

Supplementary Fig. 8. Displacement of 1NN atoms of vacancy site in $Ni_{100-x}Mo_x$ alloys in **a,** initial and **b,** final state of vacancy migration. The error bars represent the standard error from 5,000 independent simulations.

Supplementary Fig. 9 shows the trajectory of a single vacancy in $Ni_{80}Mo_{10}W_{10}$ simulated at 1000 K for 5 ns, revealing more pronounced vacancy trapping compared to $Ni_{80}Mo_{20}$, which corroborates our analysis.

Supplementary Fig. 9. Trajectory of single vacancy diffusion in $Ni_{80}Mo_{10}W_{10}$ at 1000 K for 5ns.

Supplementary Note VII. Densely distributed small defects as effective defect sinks

The morphologies of all defects, including isolated point defects and clusters of various sizes, are presented in **Supplementary Fig. 10a**. Their corresponding defect size distributions are shown in **Supplementary Fig. 10b**.

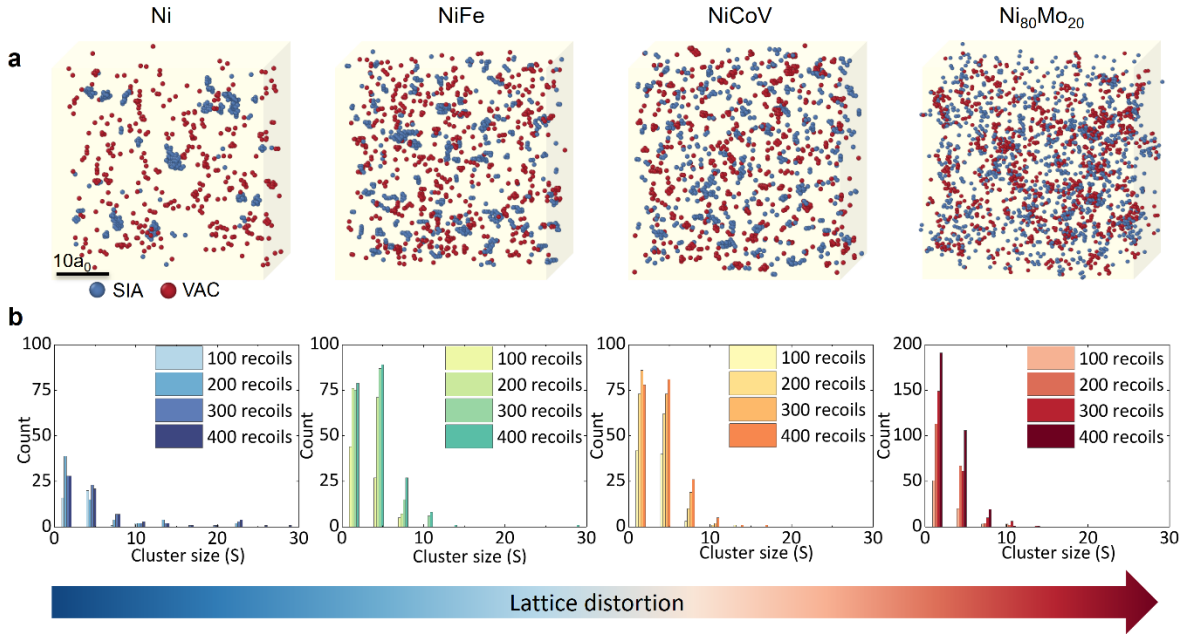

Supplementary Fig. 10. a, Morphology of defects (including point defects) after 400 recoils in Ni, NiFe, NiCoV, and $Ni_{80}Mo_{20}$. Blue and red spheres represent the interstitials and vacancies,

respectively. **b,** Defect size distribution in Ni, NiFe, NiCoV, and $Ni_{80}Mo_{20}$ as a function of number of recoils at 300 K.

The creation relaxation algorithm (CRA) was employed to study the defect distribution at high dpa level in a 30×30×30 FCC lattice. **Supplementary Fig. 11** illustrates the defect morphologies in Ni and $Ni_{80}Mo_{20}$ at 10 dpa, along with the evolution of their cluster size distributions as a function of dpa. The results show good agreement with our cascade overlap simulations and irradiation experiments, where large size defects are found in Ni, while isolated point defects and small clusters are dominant in $Ni_{80}Mo_{20}$.

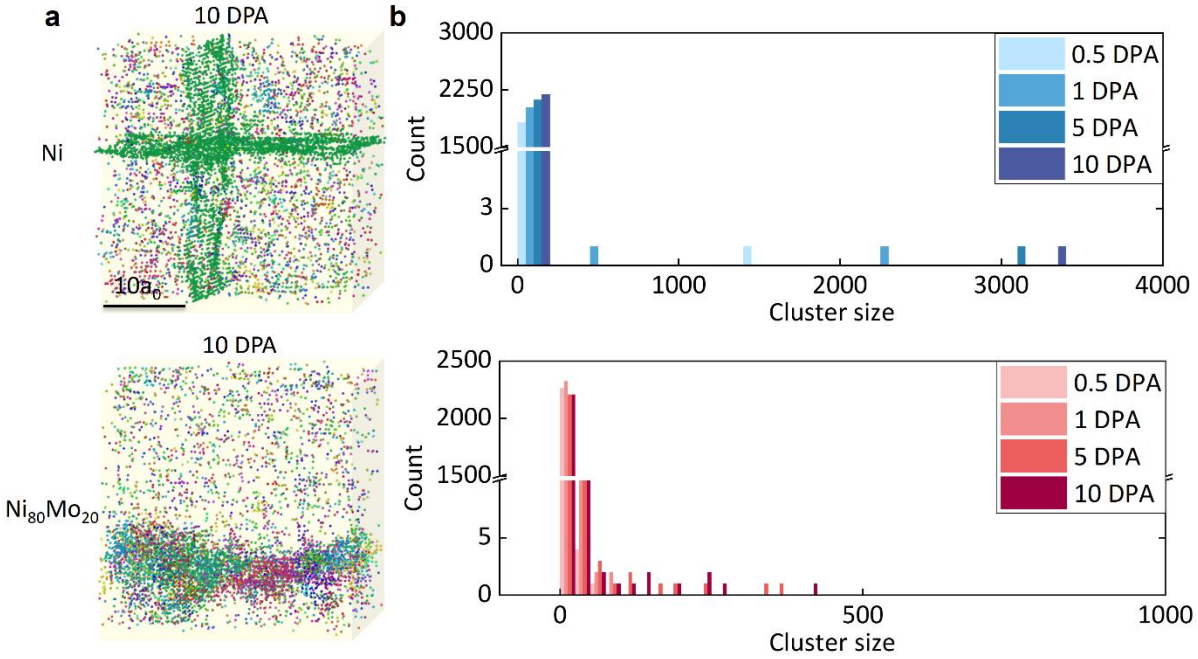

Supplementary Fig. 11. a, Morphology of defects in Ni and $Ni_{80}Mo_{20}$ at 10 dpa. **b,** Evolution of defect cluster size distribution with the increase of dpa. Distinct colors in panel **a** represent different defect-cluster IDs.

Previous study has indicated that these dense point defects or small defect clusters can act as effective defect sinks[4]. To quantify the sink ability of these defects, we assessed the sink strength of the survival defects after 400 recoils in Ni, NiFe, NiCoV, and $Ni_{80}Mo_{20}$. Specifically, the sink strength is calculated as[5]:

$$k^2 = k_i^2 + k_V^2 = \frac{\rho_i}{\frac{a^2}{2\pi R_i^2} + \frac{ln\,(\Re/R_i)}{2\pi}} + \frac{4\pi R_V \rho_V}{1 + a/R_V} \tag{8}$$

where k_i^2 and k_V^2 are the sink strength of interstitials and vacancies, respectively. ρ_i is the

density of interstitials, a is the lattice constant. $\Re$ and R_i are capture volume radius and sink radius of interstitials, respectively. $\Re$ is calculated as $(\pi\Re^2)\rho_i = 1$. R_V represents the sink radius and ρ_V is the density of vacancies. Please see more detailed descriptions in Ref.[5].

The density and size of the interstitials and vacancies are shown in **Supplementary Table 3**. The obtained sink strength in these four materials is illustrated in **Supplementary Fig. 12**. The results revealed that the densely distributed defects, although with small sizes, contribute significantly to defect sink strength. Thus, they can act as effective defect recombination centers.

Supplementary Table 3. Average R_i, ρ_i, R_V, and ρ_V in Ni, NiFe, NiCoV, and $Ni_{80}Mo_{20}$ after 400 recoils.

	R_i (m)	ρ_i (m^{-2})	R_V (m)	ρ_V (m^{-3})
Ni	5.58×10^{-10}	2.73×10^{15}	1.43×10^{-10}	8.35×10^{24}
NiFe	2.11×10^{-10}	4.48×10^{15}	1.51×10^{-10}	1.45×10^{25}
NiCoV	1.84×10^{-10}	2.91×10^{15}	1.80×10^{-10}	1.72×10^{25}
$Ni_{80}Mo_{20}$	1.23×10^{-10}	2.58×10^{15}	1.39×10^{-10}	3.11×10^{25}

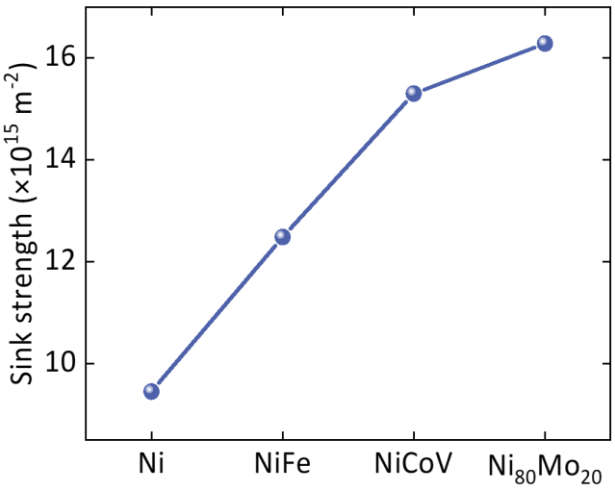

Supplementary Fig. 12. Sink strength of defects in Ni, NiFe, NiCoV, and $Ni_{80}Mo_{20}$.

Supplementary Note VIII. Irradiation hardening

To assess the impact of the high density of point defects on irradiation hardening, the dispersed barrier hardening model developed by Seeger *et al.*[6] was employed:

$$\Delta\sigma = \alpha M \mu b \sqrt{Nd} \tag{9}$$

where $\Delta\sigma$ is the yield strength change, M is the Taylor factor (3.06 for FCC metals), μ is the shear modulus (77.8 GPa in this study[7]), b is the Burgers vector magnitude ($b = a/\sqrt{2}$, with a as the lattice parameter), N is the defect number density, and d is the defect diameter.

The obstacle strength factor (α) was calculated using the model from Ref.[8]:

$$\alpha = \frac{0.271A}{(1-\nu)^{\frac{1}{2}}\sqrt{ND}(16-\pi tA)} \ln\left(\frac{0.637D}{r_0}\right) \tag{10}$$

Here, t is the thin plate thickness, with a value of 0.207 nm, r_0=b[7], and A is given as:

$$A = \sqrt{16\pi ND} + 4ND^2 - \pi^2 NDt \tag{11}$$

Defect density (N) was determined as $\frac{Average\ number\ of\ clusters}{V_{simulation\ cell}}$, and defect diameter ($D$) was calculated using $D = N_{def} \times \frac{3}{2\pi}(V_{atomic})^{\frac{1}{3}}$, where N_{def} is the average number of defects in a cluster.

Supplementary Table 4 shows the Average number of clusters ($N_{cluster}$), cluster number density (N), average number of defects in clusters (N_{def}), and cluster size (D) in Ni, NiFe, NiCoV, and $Ni_{80}Mo_{20}$ resulting from 400 recoils.

Supplementary Table 4. Average number of clusters composed of both interstitials and vacancies ($N_{cluster}$), cluster number density (N), average number of defects in clusters (N_{def}), and cluster size (D) in Ni, NiFe, NiCoV, and $Ni_{80}Mo_{20}$.

	$N_{cluster}$	Number density (N) ($\times 10^{22}\ m^{-3}$)	N_{def}	Cluster size (D) (nm)
Ni	70	1.27×10^3	6.46	1.61

NiFe	205	3.57×10^3	3.80	0.96
NiCoV	192	3.30×10^3	3.71	0.94
$Ni_{80}Mo_{20}$	354	5.86×10^3	2.8	0.72

Supplementary Fig. 13 shows their obstacle strength factors and hardening levels. Despite the high point defect density in $Ni_{80}Mo_{20}$, its significantly smaller cluster size results in lower hardening compared to other materials, indicating a minimal effect of point defects on hardening.

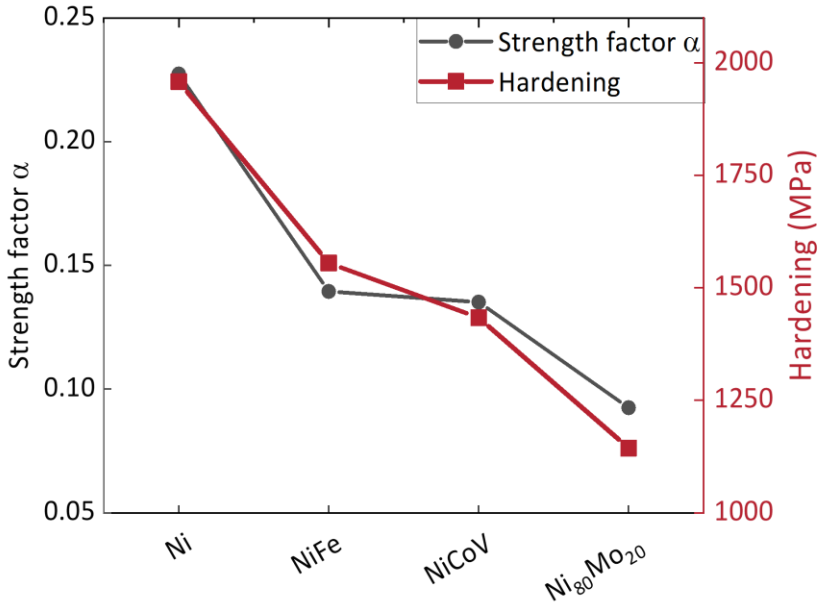

Supplementary Fig. 13. Strength factor and hardening in Ni, NiFe, NiCoV, $Ni_{80}Mo_{20}$ after 400 recoils.

Supplementary References

1 Zhang, Z. *et al.* Effect of local chemical order on the irradiation-induced defect evolution in CrCoNi medium-entropy alloy. *Proceedings of the National Academy of Sciences* **120**, e2218673120 (2023).

2 Shi, T. *et al.* Distinct point defect behaviours in body-centered cubic medium-entropy alloy NbZrTi induced by severe lattice distortion. *Acta Materialia* **229**, 117806 (2022).

3 Luo, Z., Gao, W. & Jiang, Q. Determinants of vacancy formation and migration in high-entropy alloys. *Science Advances* **11**, eadr4697 (2025).

4 Zinkle, S. J. & Snead, L. L. Designing radiation resistance in materials for fusion energy. *Annual Review of Materials Research* **44**, 241-267 (2014).

5 Was, G. S. *Fundamentals of radiation materials science: Metals and alloys*. (springer, 2016).

6 Seeger, A., Diehl, J., Mader, S. & Rebstock, H. Work-hardening and work-softening of face-centred cubic metal crystals. *The Philosophical Magazine: A Journal of Theoretical Experimental and Applied Physics* **2**, 323-350 (1957).

7 Tan, L. & Busby, J. T. Formulating the strength factor α for improved predictability of radiation hardening. *Journal of Nuclear Materials* **465**, 724-730 (2015).

8 Zhu, P., Zhao, Y., Lin, Y.-R., Henry, J. & Zinkle, S. J. Defect-specific strength factors and superposition model for predicting strengthening of ion irradiated Fe18Cr alloy. *Journal of Nuclear Materials* **588**, 154823 (2024).